Floquet Chern insulators of light

Li He[1], Zachariah Addison[1], Jicheng Jin[1], Eugene J. Mele[1], Steven G. Johnson[2] & Bo Zhen[1]

Achieving topologically-protected robust transport in optical systems has recently been of great interest. Most studied topological photonic structures can be understood by solving the eigenvalue problem of Maxwell's equations for static linear systems. Here, we extend topological phases into dynamically driven systems and achieve a Floquet Chern insulator of light in nonlinear photonic crystals (PhCs). Specifically, we start by presenting the Floquet eigenvalue problem in driven two-dimensional PhCs. We then define topological invariant associated with Floquet bands, and show that topological band gaps with non-zero Chern number can be opened by breaking time-reversal symmetry through the driving field. Finally, we numerically demonstrate the existence of chiral edge states at the interfaces between a Floquet Chern insulator and normal insulators, where the transport is non-reciprocal and uni-directional. Our work paves the way to further exploring topological phases in driven optical systems and their optoelectronic applications.

---

[1] Department of Physics and Astronomy, University of Pennsylvania, Philadelphia, PA 19104, USA. [2] Department of Mathematics, Massachusetts Institute of Technology, Cambridge, MA 02139, USA. Correspondence and requests for materials should be addressed to B.Z. (email: bozhen@sas.upenn.edu)

The field of topological photonics seeks to classify and demonstrate various topological phases in Maxwell's equations, and to apply their associated robust states in optical systems[1–3]. Though initially inspired by progress in electronic systems, topological photonics has recently developed in multiple directions using its unique ingredients, such as the easy incorporation of non-Hermiticity via material gain[4–6] or radiative loss[7]. Many important applications of topological photonics, such as optical isolators and circulators, are non-reciprocal in nature, which means they are exclusive for topological phases in systems with broken time-reversal symmetry. In static structures, such topological phases are often achieved by starting with engineered degeneracies between two bands of a PhC—in an either linear (Dirac) or quadratic fashion—followed by a static perturbation that breaks reciprocity, such as gyromagnetic effects[8–11]. The resulting systems are often referred to as Chern insulators, as their topological gaps can support uni-directional modes, whose transport is protected by the topological invariant of Chern numbers. Another important method to break reciprocity is through temporal modulation[12], yet the understanding of topological phases in dynamically driven optical systems is often limited to tight-binding models of coupled resonators[13–15] or waveguides[16–18].

Here, we study Floquet topological phases in general nonlinear PhCs under external drive and show how non-reciprocal transport can be achieved in a Floquet Chern insulator. We start by formulating the Floquet eigenvalue problem of Maxwell's equations, and show it is necessarily non-Hermitian but with real eigenvalues in many cases. After elucidating what time-reversal symmetry (T) entails in driven systems, we engineer the external drive to break T and to close and re-open Floquet gaps to change bands Chern numbers. Finally, through numerical simulations of realistic designs, we present an explicit example of a Floquet Chern insulator, along with the dispersions and locations of uni-directional chiral edge states at its interfaces with normal insulators.

Results

Floquet gaps and Floquet eigenvalue problem. We start by showing that new bandgaps—Floquet gaps—can be created in driven nonlinear PhCs, which do not exist in the static band structure. We consider a two-dimensional PhC that involves second-order optical nonlinear materials such as $LiNbO_3$. The static band structure is schematically shown in Fig. 1b, and we focus on two isolated bands: $|1\rangle$ in blue and $|2\rangle$ in red, which are separated by a gap in the spectrum. When an external driving
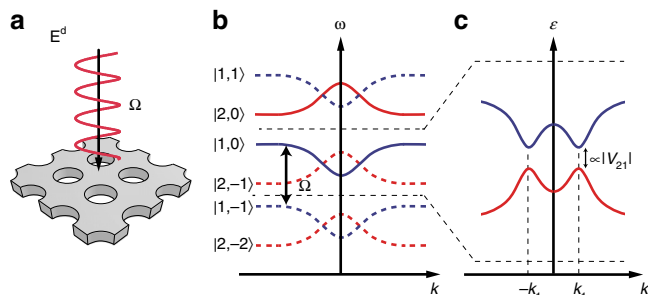
field at frequency Ω is applied along the normal direction, the discrete spatial translation symmetry of the system is preserved, but the continuous temporal translation symmetry is broken, leaving only a discrete temporal translation symmetry. Accordingly, each band creates copies of itself—Floquet bands—shifted up or down in the spectrum by $m\Omega$, where m is an integer. When Ω is slightly larger than the static gap, two of the Floquet bands, $|1, m = 0\rangle$ and $|2, m = -1\rangle$, cross, and the coupling between them V_{21} opens a new gap—Floquet gap—that is controlled by the driving field. When the driving field is weak, the size of the Floquet gap is linearly proportional to the coupling strength $|V_{21}|$, meaning this gap can only be closed at momentum ($\mathbf{k}$) points where the complex coupling term vanishes: $V_{21}(\mathbf{k}) = 0$. We later show these singular points represent the topological phase transitions between Floquet Chern insulators and normal insulators.

Next, we present the Floquet eigenvalue problem of Maxwell's equations in this system. The result (Eqs. (1a) and (1b)) is achieved by adding time-dependent nonlinear permittivity tensor $\overline{\overline{\epsilon}}_{nl}(t)$—determined by both the nonlinear material and the driving field—into the static eigenvalue problem[1].

$$A\Psi = i\partial_t[(B_0 + B_{nl})\Psi] \tag{1a}$$

$$A = \begin{pmatrix} 0 & i\nabla\times \\ -i\nabla\times & 0 \end{pmatrix}, B_0 = \begin{pmatrix} \overline{\overline{\epsilon}}_1 & 0 \\ 0 & \mu_0 \end{pmatrix}, B_{nl} = \begin{pmatrix} \overline{\overline{\epsilon}}_{nl}(t) & 0 \\ 0 & 0 \end{pmatrix} \tag{1b}$$

where $\overline{\overline{\epsilon}}_1$ is the linear permittivity tensor, and $\Psi(t) = (\mathbf{E}, \mathbf{H})^T$ are the complex electromagnetic fields. Here, we focus on instantaneous nonlinear processes and assume all materials involved are dispersion-less and loss-less for simplicity, although dispersive medium can potentially also be included[19]. Compared to the Floquet eigenvalue problem of Schrödinger equation[20–22], our problem is different in a few unique ways. First, it is necessarily non-Hermitian, as the $i\partial_t$ term cannot commute with the $B_{nl}(t)$ term on the right hand side of Eq. (1a), though each individual term is Hermitian. Second, interestingly, the Floquet eigenvalues can be guaranteed as real under some conditions discussed later. We solve the Floquet states $\Psi(t)$, which are the eigenstates of this linear eigenvalue problem, by expanding them in the Floquet basis $|j, m\rangle = |j\rangle e^{im\Omega t}$ as $\Psi(t) = e^{i\mathbf{k}\cdot\mathbf{r}-i\varepsilon t}\sum_{jm}c_{jm}|j, m\rangle$. Here, ε is the quasi-energy; $|j\rangle$ satisfies the static eigenvalue problem of $e^{-i\mathbf{k}\cdot\mathbf{r}}Ae^{i\mathbf{k}\cdot\mathbf{r}}|j\rangle = \omega_j B_0|j\rangle$ and therefore forms a complete basis of spatial modes. Similar approach has also been used in solving the Floquet eigenstates of periodic paraxial equations[23,24]. The detailed solution is presented in Supplementary Note 1 with discussions in Note 2.

Topological defects in momentum space. To better illustrate some of the key concepts, we focus on an example when two bands become close to each other under driving $\omega_2 - \omega_1 \approx \Omega$, while both are far away from other bands. Hence, we restrict the trial solutions to the subspace spanned by the two bands for simplicity; however, the presented formalism is general and not limited to the two-band model. Under a further rotating-wave approximation, the Floquet eigenvalue problem can be simplified into:

$$\begin{pmatrix} \omega_2 - \Omega & -\Omega V_{21} \\ 0 & \omega_1 \end{pmatrix}\begin{pmatrix} c_{2,-1} \\ c_{1,0} \end{pmatrix} = \varepsilon\begin{pmatrix} 1 & V_{21} \\ V_{21}^* & 1 \end{pmatrix}\begin{pmatrix} c_{2,-1} \\ c_{1,0} \end{pmatrix}. \tag{2}$$

As shown, this generalized eigenvalue problem is indeed non-Hermitian, but its eigenvalues can be guaranteed as real under some conditions. For example, when the driving field is exactly

Fig. 1 Floquet bands and gaps in a periodically driven nonlinear photonic crystal. **a** Schematic of a nonlinear photonic crystal (PhC) placed in a monochromatic driving field $\mathbf{E}^d$ at frequency Ω. **b** Due to the periodic drive, static bands of the PhC (solid lines) create copies of themselves—Floquet bands (dashed lines)—by shifting up or down in the spectrum. **c** Two of the Floquet bands $|1, m = 0\rangle$ and $|2, m = -1\rangle$ cross at $\pm k_1$. Their coupling term V_{21} opens a new gap E_g—Floquet gap—and its size is linearly proportional to the magnitude of their coupling strength $|V_{21}|$ under weak drive

on-resonance, namely $\omega_2 = \omega_1 + \Omega$, the two Floquet eigenvalues can be further simplified as: $\varepsilon_{\pm} \approx \omega_1 \pm 2|V_{21}|\sqrt{\omega_1\omega_2}$. The normalized gap size is linearly proportional to $|V_{21}|$, whose magnitude is determined by both the modal overlap and the driving field strength. Furthermore, we note that both eigenvalues are necessarily real as long as we are coupling bands both at positive (or negative) frequencies ($\omega_1\omega_2 > 0$). Physically, these scenarios are analogous to the depletable sum-frequency generation: power oscillates between a depletable pump ω_1 and the sum-frequency beam ω_2, but their total photon number remains fixed in time[25,26]. On the other hand, complex eigenvalues may appear when a positive-frequency mode is coupled to a negative-frequency mode ($\omega_1\omega_2 < 0$) and the resulting Floquet modes may grow exponentially in time. These scenarios are analogous to optical parametric amplification where a non-depletable pump beam ($|\omega_1| + |\omega_2|$) amplifies the signal and idler beams[26]. In this Letter, we focus on the first situation where Floquet eigenvalues are real. Topological phase transitions can only happen at $\mathbf{k}$ points where the gap is closed, requiring the coupling term $V_{21} = 0$. This is equivalent to requiring the complex phase $\arg V_{21}$ to be undefined, or to be a topological defect[27], in $\mathbf{k}$ space. The topological phase transitions, being topological defects, are thus robust against any perturbations that modify the complex coupling terms V_{21}, as such perturbations cannot get rid of the topological phase transitions but shift their positions in the 3D parameter space of (k_x, k_y, Ω).

Next, we show how such topological defects can be synthesized by engineering the polarization of the driving field. Our considered PhC sample is shown in Fig. 2a, which is consisted of a hexagonal lattice, with lattice constant a, of regions made of silicon ($\epsilon = 12.25$) and regions made of z-cut LiNbO$_3$ ($\epsilon_{xx} = \epsilon_{yy} = 4.97$, $\epsilon_{zz} = 4.67$). Both inversion and rotation symmetries are broken to lift all degeneracies at high-symmetry $\mathbf{k}$ points. The static band structure is calculated using Finite Element Methods (see Methods section for details) and shown in Fig. 2b. In the static structure, TE bands (H_z, E_x, E_y; red) are decoupled from the TM bands (E_z, H_x, H_y; blue), due to the mirror symmetry in the z direction. However, under a driving field polarized in the xy plane, TE and TM bands are coupled: specifically, the external field $E_{x,y}^d$ drives the second-order optical nonlinearity of LiNbO$_3$, $\chi_{zxx}^{(2)}$ and $\chi_{zyy}^{(2)}$, and creates $\epsilon_{xz,zx}$ and $\epsilon_{yz,zy}$ terms in the effective permittivity tensor of LiNbO$_3$. These four terms break the mirror symmetry in z and couple the E_z component of a TM mode to the $E_{x,y}$ components of a TE mode. By analyzing the nonlinear optical property of LiNbO$_3$, one can show only TE-TM bands are coupled via modulation in this setup, while the Floquet TE-TE or TM-TM bands will not couple to each other (see Methods for details).

We found that time-reversal symmetry (T) in the Floquet eigenvalue problem is defined as $V_{21}(\mathbf{k}) = V_{21}^{\star}(-\mathbf{k})$. Furthermore, we found T is preserved when the driving field is linearly polarized and no topological Floquet gap can be opened. On the other hand, elliptically polarized driving fields break T. The condition on T in these two scenarios can be intuitively understood by analyzing the temporal evolution of the instantaneous optical principle axes of LiNbO$_3$: under a linearly polarized monochromatic drive, one optical axis remains static, while the other two oscillate in a time-reversal symmetric manner. In comparison, under an elliptically polarized drive, all three optical axes rotate around the z axis at the driving frequency and this spinning behavior breaks T. Detailed derivation is presented in Supplementary Notes 4 and 5.

The properties associated with time-reversal symmetry are confirmed in our simulation results of the modal coupling terms V_{21} as shown in Fig. 2c, d. Specifically, under a linearly polarized
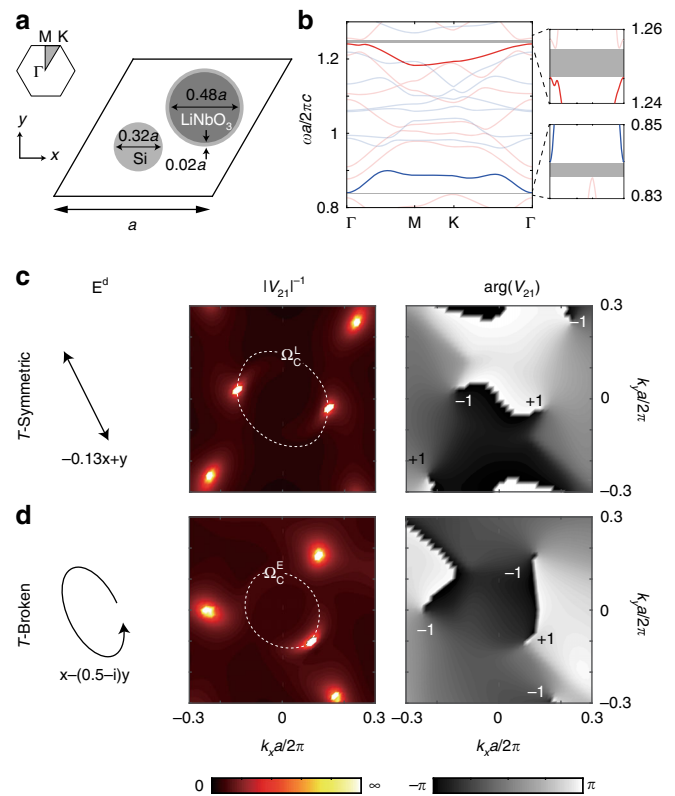

Fig. 2 Topological charges in modal coupling terms and the influence of time-reversal symmetry. **a** Nonlinear PhC unit cell involving Si and z-cut LiNbO$_3$. The centers of the Si and LiNbO$_3$ rods are at $(0.55a\hat{\mathbf{x}} + a/2\sqrt{3}\hat{\mathbf{y}})$ and $(a\hat{\mathbf{x}} + a/\sqrt{3}\hat{\mathbf{y}})$ with respect to the bottom-left corner of the unit cell. **b** Static modes are separated into TE (red) and TM (blue) bands. Under a driving field polarized in the xy plane, a TE band is coupled to a TM band through $\chi^{(2)}$ of LiNbO$_3$. Their coupling term V_{21} is controlled by the polarization of the drive. **c** Under a linearly polarized drive $(-0.13\hat{\mathbf{x}} + \hat{\mathbf{y}})$, pairs of vortices with opposite topological charges (± 1) are found in the complex phase $\arg V_{21}$, located at opposite $\mathbf{k}$ points. At these $\mathbf{k}$ points, the modal coupling term vanishes and $1/|V_{21}| \to \infty$. **d** Under an elliptically polarized drive, $\hat{\mathbf{x}} - (0.5 - i)\hat{\mathbf{y}}$, vortices in $\arg V_{21}$ appear without any symmetry. Topological phase transition is achieved between a Floquet normal insulator and a Floquet Chern insulator through a single topological charge at Ω_C^E (dashed circle)

drive (T-symmetric), V_{21} reduces to 0 at pairs of opposite $\mathbf{k}$ points that are related by T-symmetry, shown as bright spots in Fig. 2c. Furthermore, each pair of topological defects carry opposite topological charges q, which are defined through the winding numbers of the complex phase:

$$q = \frac{1}{2\pi} \oint_C d\mathbf{k} \cdot \nabla_{\mathbf{k}} \arg V_{21}. \tag{3}$$

Here C is a closed path in $\mathbf{k}$ space that encircles the defect in the counter-clockwise direction. Consequently, the Floquet gap can be closed and re-opened by tuning the driving frequency through a critical value $\Omega_C^L a/2\pi c = 0.375$ (dashed circle); however, the transitions always happen at a pair of opposite $\mathbf{k}$ points and the Floquet bands are always topologically trivial. See Supplementary Note 6 for the definition of Berry curvature and Chern number of Floquet bands. On the other hand, under an elliptically polarized drive (T-broken), topological defects appear without any symmetry (Fig. 2d). As a result, the Floquet gap can close and re-open at a single $\mathbf{k}$ point, as $V_{21}(\mathbf{k})$ is no longer related to
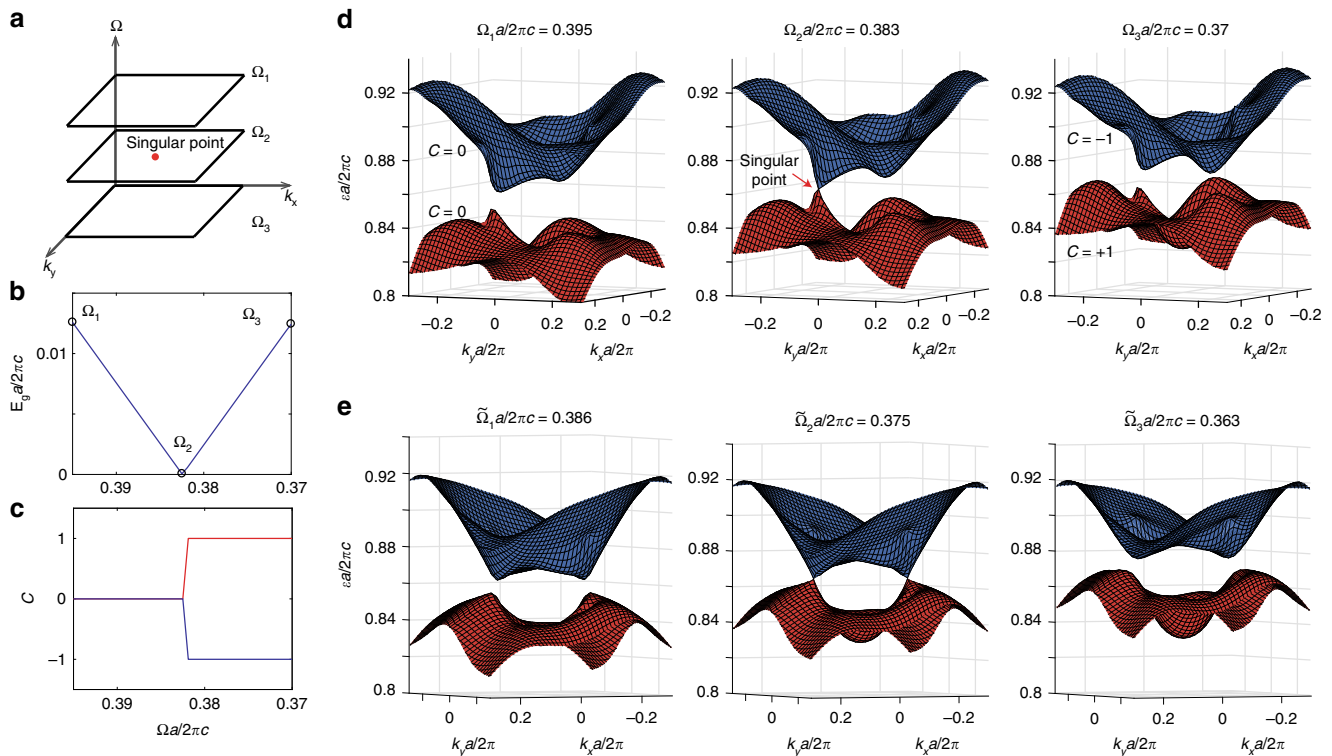
Fig. 3 Topological phase transition points in 3D synthetic parameter space. **a** The topological phase transition point is defined in the parameter space of (k_x, k_y, Ω). **b** Under an elliptically polarized drive, the Floquet band gap closes at $\Omega_2 a/2\pi c = 0.383$, and increases linearly in its vicinity on both sides. Here we plot the partial gap size defined as the minimum of partial gap in the **k** space. **c** Under an elliptically polarized drive, the Chern numbers of the top (blue) and bottom band (red) change by 1 as Ω scans through Ω_2. **d** The Floquet band structure shows a linear touching between the top and bottom bands at a singular **k** point at Ω_2 (middle panel). This singular point represents a topological phase transition between a Floquet normal insulator (Ω_1, left) and a Floquet Chern insulator (Ω_3, right). **e** In contrast, the Floquet band gap closes and re-opens at a pair of opposite **k** points for T-symmetric drive when tuning driving frequency from $\tilde{\Omega}_1$ to $\tilde{\Omega}_3$ and is thus topologically trivial

$V_{21}(-\mathbf{k})$. In our system, this topological phase transition happens at another critical value $\Omega_C^E a/2\pi c = 0.381$ (dashed circle).

Topological phase transition through unpaired topological defects. Next, we study topological phase transitions between Floquet Chern insulators and normal insulators and show these transition points are singular points in the parameter space of (k_x, k_y, Ω) as shown in Fig. 3a. First, the Floquet band gap closes at the transition point, but grows linearly as Ω deviates from Ω_2 (Fig. 3b). Furthermore, we compare the Floquet spectra near the transition point: the bands are gapped when either $\Omega > \Omega_2$ (left panel of Fig. 3d) or $\Omega < \Omega_2$ (right); however, the two Floquet bands touch at a singular point in **k** space in a linear fashion when $\Omega = \Omega_2$ (middle). We note the small difference between Ω_2 and Ω_C^E arises from the difference between full Floquet formulation we adopt here and results under rotating-wave approximation. The gap size grows linearly as the system parameter deviates from a single point in the three-dimensional parameter space of (k_x, k_y, Ω), therefore, the transition points can also be interpreted as synthetic Weyl points[28–31]. We further track the Chern numbers of the Floquet bands as Ω is varied: the Chern number of the top (bottom) band changes by −1 (1) as the modulation frequency reduced from $\Omega_1 a/2\pi c = 0.395$ (Floquet normal insulator) to $\Omega_3 a/2\pi c = 0.37$ (Floquet Chern insulator), through $\Omega_2 a/2\pi c = 0.383$ (Fig. 3c). In addition, the Chern numbers of the two bands jump in opposite directions with their sum fixed at 0, which confirms our system is a Chern insulator. Similarly, the Floquet gap can also be closed and re-opened under linearly polarized driving fields. For example, by tuning Ω

through a critical value of $\tilde{\Omega}_2 a/2\pi c = 0.375$, the Floquet gap is closed and re-opened, but at a pair of opposite **k** points. Through this process, all bands remain topologically trivial with zero Chern numbers due to the presence of T-symmetry.

Chiral edge states induced by driving field. Finally, we show the existence of chiral edge states at the interfaces between a Floquet Chern insulator (gray region in Fig. 4a) and normal insulators (white region). In this super-cell geometry, we apply periodic boundary conditions in both x and y directions, and these two insulators have two interfaces, top and bottom. The topological region shares the same setup as the right panel of Fig. 3d; the trivial region is driven at the same frequency $\Omega_3 a/2\pi c = 0.37$, but with a linearly polarized light ($\hat{\mathbf{x}} + 0.3\hat{\mathbf{y}}$) that preserves T. Through a super-cell calculation (Supplementary Note 7), all bands in the system are computed. Aside from the bulk bands in the trivial and nontrivial regions, we see chiral edge states (red and blue lines) emerge at the two interfaces with frequencies going across the topological band gap. Their mode profiles further confirm these are indeed edge states localized at the top (red) and bottom (blue) interfaces (Fig. 4c); in comparison, a bulk mode (black) is delocalized along the y-direction. As a control experiment, when the driving frequency is changed to Ω_1 such that all regions are topologically trivial, no gapless chiral edge state is observed in such scenario (Fig. 4d). This confirms the number of chiral edge states and their traveling directions are consistent with the Floquet topological band theory results for electronic systems[32]. We note that the photon number is conserved in edge state transport. This is to be distinguished from a
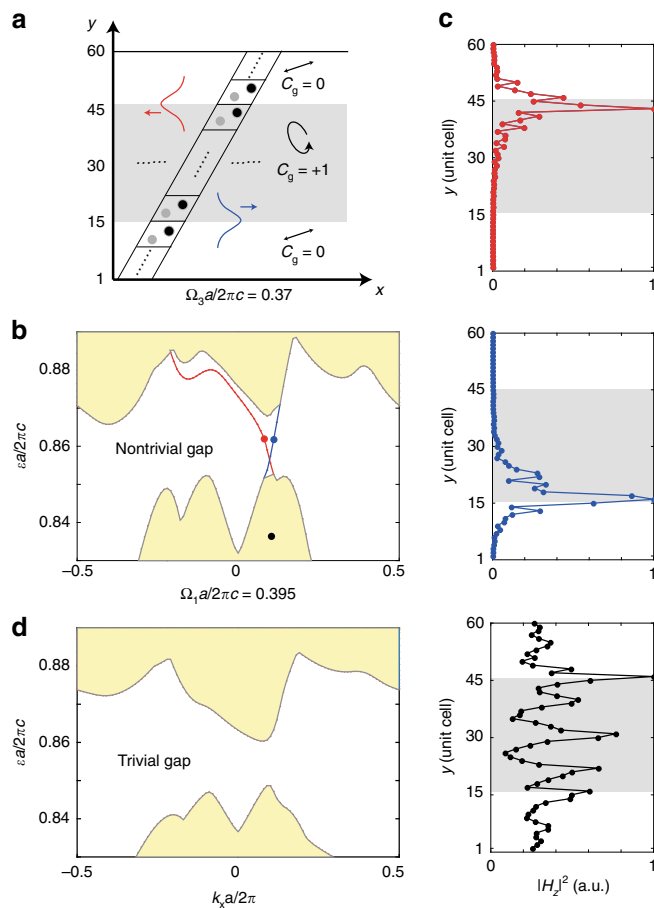
Fig. 4 Characterizations of chiral edge states at the interfaces between a Floquet Chern insulator and normal insulators. **a** Schematic of the super-cell geometry with a Floquet Chern insulator placed in between two Floquet normal insulators. The Floquet Chern insulator is the same setup as the right panel of Fig. 3d. All regions are driven at the same frequency Ω_3, and the associated gap Chern number for the Floquet insulator is $C_g = 1$. Further details of the super-cell setup can be found in Supplementary Note 7. **b** The dispersion along k_x axis shows two types of modes: bulk bands in the normal and Chern insulator regions (yellow) and uni-directional chiral edge states at the top and bottom interfaces (red and blue). **c** Chiral edge states are absent in the projected dispersion when all regions are driven at frequency Ω_1 before the topological phase transition. **d** Comparison among the mode profiles of a bulk state (black), the chiral edge states localized at the top interface traveling to the left (red) and at the bottom interface traveling to the right (blue)

previous study using nonlinear parametric driving by Peano et al.[33], where the photon number is not conserved, and the edge state transport becomes inelastic. Although helical spatial modulation of waveguide arrays achieves Floquet Chern insulators in the transverse plane[16], our approach breaks reciprocity for the system as a whole and thus enables optical isolation through the chiral edge states.

Discussion

To sum up, we present a general framework to achieve Floquet topological phases in nonlinear photonic crystals, defined by the Floquet eigenvalue problems in Maxwell's equations. We show that Floquet band gaps can be closed and re-opened in a virtually arbitrary fashion by engineering the driving field (polarization and frequency). Using this framework, we propose and numerically

demonstrate a Floquet Chern insulator of light by breaking time-reversal symmetry using elliptically polarized driving fields. We show the Floquet topological phase transitions are through singular points of modal coupling terms in 3D parameter space. Finally, we numerically demonstrate the existence of chiral edge states at the interfaces between topologically trivial and non-trivial regions. Our work paves the way to further classifying and realizing topological phases in dynamically driven optical systems and their optoelectronic applications in communication and signal routing. Our method of inducing Floquet topological phases is also applicable to other wave systems, such as phonons, excitons, and polaritons.

Note added: During the completion of this work, we became aware of a related study by Fang and Wang[34].

Methods

Numerical simulation of Maxwell equation using Finite Element Methods. The band structures and mode profiles are calculated using Finite Element Methods in COMSOL Multiphysics 5.3a. Specifically, we first compute the static band structures and mode profiles using the linear permittivity in a 2D geometry with periodic boundary conditions. The modal overlaps $V_{21}(\mathbf{k})$ are calculated by taking the inner product between the two modes mediated by external drive and nonlinear susceptibility of the LiNbO$_3$. Finally, we input these coupling terms into the master equation (Supplementary Eq. (4)) to calculate the eigenvalues, mode profiles, Berry curvature, and Chern numbers of the Floquet bands.

Band coupling via the second-order optical nonlinearity of LiNbO$_3$. Under an driving field polarized in the xy plane, TE-TM bands are coupled to each other through $\chi^{(2)}_{zxx}$ (d_{31}) and $\chi^{(2)}_{zyy}$ (d_{32}) terms of LiNbO$_3$, both of which are 5 pm·V^{-1}[35]. On the other hand, the E_z components of TM modes cannot couple to each other via modulation, because the relevant terms, $\chi^{(2)}_{zxz}$ and $\chi^{(2)}_{zyz}$, are both 0 in LiNbO$_3$. Similarly, the $E_{x,y}$ components of TE modes cannot couple via modulation either. The resulted Floquet gap size due to band coupling is linearly proportional to both the $\chi^{(2)}$ coefficients and the driving field strength. We present the estimation on the Floquet gap size that can be possibly achieved in realistic nonlinear materials in Supplementary Note 8.

Data availability

The data that support the findings of this study are available from the corresponding author upon reasonable request.

References

1. Lu, L., Joannopoulos, J. D. & Soljačić, M. Topological photonics. *Nat. Photonics* **8**, 821 (2014).
2. Khanikaev, A. B. & Shvets, G. Two-dimensional topological photonics. *Nat. Photonics* **11**, 763 (2017).
3. Ozawa, T. et al. Topological photonics. *Rev. Mod. Phys.* **91**, 015006 (2019).
4. Bandres, M. A. et al. Topological insulator laser: experiments. *Science* **359**, eaar4005 (2018).
5. Bahari, B. et al. Nonreciprocal lasing in topological cavities of arbitrary geometries. *Science* **358**, 636–640 (2017).
6. Peano, V., Houde, M., Marquardt, F. & Clerk, A. A. Topological quantum fluctuations and traveling wave amplifiers. *Phys. Rev. X* **6**, 041026 (2016).
7. Zhou, H. et al. Observation of bulk fermi arc and polarization half charge from paired exceptional points. *Science* **359**, 1009–1012 (2018).
8. Wang, Z., Chong, Y., Joannopoulos, J. D. & Soljačić, M. Reflection-free one-way edge modes in a gyromagnetic photonic crystal. *Phys. Rev. Lett.* **100**, 013905 (2008).
9. Wang, Z., Chong, Y., Joannopoulos, J. D. & Soljačić, M. Observation of unidirectional backscattering-immune topological electromagnetic states. *Nature* **461**, 772 (2009).
10. Haldane, F. & Raghu, S. Possible realization of directional optical waveguides in photonic crystals with broken time-reversal symmetry. *Phys. Rev. Lett.* **100**, 013904 (2008).
11. Skirlo, S. A. et al. Experimental observation of large chern numbers in photonic crystals. *Phys. Rev. Lett.* **115**, 253901 (2015).

12. Jalas, D. et al. What is–and what is not–an optical isolator. *Nat. Photonics* **7**, 579 (2013).

13. Yuan, L. & Fan, S. Bloch oscillation and unidirectional translation of frequency in a dynamically modulated ring resonator. *Optica* **3**, 1014–1018 (2016).

14. Lin, Q., Sun, X.-Q., Xiao, M., Zhang, S.-C. & Fan, S. A three-dimensional photonic topological insulator using a two-dimensional ring resonator lattice with a synthetic frequency dimension. *Sci. Adv.* **4**, eaat2774 (2018).

15. Li, M., Ni, X., Weiner, M., Alù, A. & Khanikaev, A. B. Topological phases and nonreciprocal edge states in non-hermitian floquet insulators. *Phys. Rev. B* **100**, 045423 (2019).

16. Rechtsman, M. C. et al. Photonic floquet topological insulators. *Nature* **496**, 196 (2013).

17. Maczewsky, L. J., Zeuner, J. M., Nolte, S. & Szameit, A. Observation of photonic anomalous floquet topological insulators. *Nat. Commun.* **8**, 13756 (2017).

18. Lustig, E., Sharabi, Y. & Segev, M. Topological aspects of photonic time crystals. *Optica* **5**, 1390–1395 (2018).

19. Raman, A. & Fan, S. Photonic band structure of dispersive metamaterials formulated as a hermitian eigenvalue problem. *Phys. Rev. Lett.* **104**, 087401 (2010).

20. Lindner, N. H., Refael, G. & Galitski, V. Floquet topological insulator in semiconductor quantum wells. *Nat. Phys.* **7**, 490 (2011).

21. Dittrich, T. et al. *Quantum Transport and Dissipation*, Vol. 3 (Wiley-Vch Weinheim, 1998).

22. D'Alessio, L. & Rigol, M. Dynamical preparation of floquet chern insulators. *Nat. Commun.* **6**, 8336 (2015).

23. Leykam, D., Rechtsman, M. C. & Chong, Y. Anomalous topological phases and unpaired dirac cones in photonic floquet topological insulators. *Phys. Rev. Lett.* **117**, 013902 (2016).

24. Plotnik, Y. et al. Analogue of rashba pseudo-spin-orbit coupling in photonic lattices by gauge field engineering. *Phys. Rev. B* **94**, 020301 (2016).

25. Winn, J. N., Fan, S., Joannopoulos, J. D. & Ippen, E. P. Interband transitions in photonic crystals. *Phys. Rev. B* **59**, 1551 (1999).

26. Boyd, R. W. *Nonlinear Optics* (Elsevier, 2003).

27. Mermin, N. D. The topological theory of defects in ordered media. *Rev. Mod. Phys.* **51**, 591 (1979).

28. Lu, L. et al. Experimental observation of weyl points. *Science* **349**, 622–624 (2015).

29. Armitage, N., Mele, E. & Vishwanath, A. Weyl and dirac semimetals in three-dimensional solids. *Rev. Mod. Phys.* **90**, 015001 (2018).

30. Lin, Q., Xiao, M., Yuan, L. & Fan, S. Photonic weyl point in a two-dimensional resonator lattice with a synthetic frequency dimension. *Nat. Commun.* **7**, 13731 (2016).

31. Wang, Q., Xiao, M., Liu, H., Zhu, S. & Chan, C. T. Optical interface states protected by synthetic weyl points. *Phys. Rev. X* **7**, 031032 (2017).

32. Rudner, M. S., Lindner, N. H., Berg, E. & Levin, M. Anomalous edge states and the bulk-edge correspondence for periodically driven two-dimensional systems. *Phys. Rev. X* **3**, 031005 (2013).

33. Peano, V., Houde, M., Brendel, C., Marquardt, F. & Clerk, A. A. Topological phase transitions and chiral inelastic transport induced by the squeezing of light. *Nat. Commun.* **7**, 10779 (2016).

34. Fang, K. & Wang, Y. Anomalous quantum hall effect of light in bloch-wave modulated photonic crystals. *Phys. Rev. Lett.* **122**, 233904 (2019).

35. Sutherland, R. L. *Handbook of Nonlinear Optics* (CRC Press, 2003).

Author contributions

L.H. and B.Z. conceived the idea. L.H. carried out numerical simulations. L.H., Z.A., J.J., E.M., S.J., and B.Z. discussed and interpreted the results. L.H and B.Z. wrote the papert with contribution from all authors. B.Z. supervised the project.

Additional information

Supplementary Information accompanies this paper at https://doi.org/10.1038/s41467-019-12231-4.

Competing interests: The authors declare no competing interests.

Reprints and permission information is available online at http://npg.nature.com/reprintsandpermissions/

Peer review information *Nature Communications* thanks the anonymous reviewer(s) for their contribution to the peer review of this work. Peer reviewer reports are available.

Publisher's note Springer Nature remains neutral with regard to jurisdictional claims in published maps and institutional affiliations.

Supplementary Information
Floquet Chern Insulators of Light

He et al.

Supplementary Note 1: Solving the Floquet eigenvalue problem by modal decomposition

In this section, we present our general formalism to solve the Floquet eigenvalue problem of a nonlinear photonic crystal driven by an external monochromatic field. According to the Floquet theorem, the trial solution for electromagnetic fields propagating in the photonic crystal can be written in the form $\Psi_{\mathbf{k}}(t) = e^{i\mathbf{k}\cdot\mathbf{r}-i\varepsilon t}\phi(t)$, where $\phi(t)$ is a periodic function in both space and time $\phi(t) = \phi(t+T)$ and T is periodicity. Substitution into Maxwell equations yields the eigenvalue problem:

$$[A_{\mathbf{k}} - i\partial_t B(t)]\phi(t) = \varepsilon B(t)\phi(t) \tag{1}$$

where $A_{\mathbf{k}} = e^{-i\mathbf{k}\cdot\mathbf{r}}Ae^{i\mathbf{k}\cdot\mathbf{r}}$, $B(t) = B_0 + B_{\mathrm{nl}}(t) = B_0 + Ve^{-i\Omega t} + V^\dagger e^{i\Omega t}$. Our method is based by decomposing the time periodic function $\phi(t)$ using the eigenstates of the static eigenvalue problem without external drive ($|j\rangle$) as $\phi(t) = \sum_{jm} c_{jm}|j\rangle e^{im\Omega} = \sum_{jm} c_{jm}|jm\rangle$ and computing the coefficients c_{jm}. To this end, we substitute the expression of $\phi(t)$ back into (1) and multiply $\langle ln|$ from the left

$$\sum_{jm} c_{jm}\langle ln|\,[A_{\mathbf{k}} - i\partial_t B(t)]\,|jm\rangle = \varepsilon\sum_{jm} c_{jm}\langle ln|\,B(t)\,|jm\rangle \tag{2}$$

Using the orthonomal condition $\langle l|\,B_0\,|j\rangle = \delta_{lj}$ and $\langle n|m\rangle = \delta_{nm}$, we obtain

$$\sum_{jm} c_{jm}[(\omega_j + n\Omega)\delta_{lj}\delta_{nm} + n\Omega V_{lj}\delta_{n,m-1} + n\Omega V_{lj}^\dagger\delta_{n,m+1}]$$
$$= \varepsilon\sum_{jm} c_{jm}(\delta_{lj}\delta_{nm} + V_{lj}\delta_{n,m-1} + V_{lj}^\dagger\delta_{n,m+1}) \tag{3}$$

where $V_{lj} = \langle l|\,V\,|j\rangle$ and $\omega_j = \langle j|\,A_{\mathbf{k}}\,|j\rangle$. Furthermore, the above equation can be casted into a matrix form

$$\hat{M}\Psi = \varepsilon\hat{N}\Psi \tag{4a}$$

2

$$\Psi = (\ldots, c_{j,-1}, c_{j,0}, c_{j,1}, \ldots)^{\mathrm{T}} \tag{4b}$$

$$\hat{M} = \begin{pmatrix} \ddots & & \ddots & & \\ -\Omega\hat{V}^\dagger & \hat{H}_0 - \Omega & -\Omega\hat{V} & \\ & 0 & \hat{H}_0 & 0 \\ & \Omega\hat{V}^\dagger & \hat{H}_0 + \Omega & \Omega\hat{V} \\ & & \ddots & & \ddots \end{pmatrix}, \quad \hat{N} = \begin{pmatrix} \ddots & \ddots & & \\ \hat{V}^\dagger & \hat{I} & \hat{V} & \\ & \hat{V}^\dagger & \hat{I} & \hat{V} \\ & & \hat{V}^\dagger & \hat{I} & \hat{V} \\ & & & \ddots & \ddots \end{pmatrix} \tag{4c}$$

with $(\hat{H}_0)_{lj} = \omega_j \delta_{lj}$. An equivalent way of writing (4a) is $\hat{N}^{-1}\hat{M}\Psi = \varepsilon\Psi$. As we expected, the matrix $\hat{M}$ on the left side of (4a) is non-Hermitian. In practice, to diagonalize the Floquet Hamiltonian, one can truncate the Fourier harmonics to a finite order ($|m| < m_c$), as the eigenstates $\{c_{jm}\}^{\mathrm{T}}$ are localized in m[1]. We set $m_c = 5$ in the calculations of both bulk and edge states dispersions. To prove the convergence, we first show c_{jm} is highly localized in m for a specific Floquet state (the bottom band at the Γ point in Fig.3d of the main text). As shown in Fig.1a, the two dominant components of c_{jm} indicate that the Floquet mode arises from the hybridization between Floquet basis $|1, m = -1\rangle$ and $|2, m = 0\rangle$, while the contributions from other Fourier orders are negligible. To further quantify the convergence of c_{jm} throughout all Floquet bands, we evaluate the worst-case scenario, defined as:

$$d(n) = \min\Big(\sum_{|m|\leq n}\sum_{j=1,2} |c_{jm}(\mathbf{k})|^2\Big) \text{ for } \mathbf{k} \in \text{B.Z.} \tag{5}$$

for the two Floquet bands in Fig.3d of the main text, respectively. The calculated $d(n)$ approaches 1 for $n \leq 2$ (Fig.1b), suggests our truncation of the Floquet basis at $m_c = 5$ is good enough for the calculation.

Supplementary Note 2: Proof of periodic spectrum

In this section, we prove the Floquet spectrum defined through (1) is necessarily periodic at the spacing of Ω. Specifically, if $\Psi_{\mathbf{k}}(t) = e^{i\mathbf{k}\cdot\mathbf{r}-i\varepsilon t}\phi(t)$ is a solution of (1) with eigenvalue ε and eigenstate $\phi(t)$, it is evident that $\Psi_{\mathbf{k}}(t) = e^{i\mathbf{k}\cdot\mathbf{r}-i(\varepsilon+\Omega)t}e^{i\Omega t}\phi(t)$ is also a solution with new eigenvalue $\tilde{\varepsilon} = \varepsilon + \Omega$ and eigenstate $\tilde{\phi}(t) = e^{i\Omega t}\phi(t) = \sum_{jm} c_{jm}\,|j,m+1\rangle = \sum_{jm}\tilde{c}_{jm}\,|j,m\rangle$, where $\tilde{c}_{jm} = c_{j,m-1}$. Compared to (4a), it implies shifting the column vector $\{c_{jm}\}^{\mathrm{T}}$ down (up) by one row also yields an eigenstate with eigenvalue increased (decreased) by Ω, though they represent the same physical state. Therefore, the resulting Floquet spectrum is periodic with a spacing of Ω.

Supplementary Note 3: Two-band simplification

In this section, we focus on a situation where only two of the bands are close to each other under the driving field ,while both bands are far away from the rest. Under rotating wave approximation, (4a) can be simplified into a series of 2-by-2 matrices by considering pairs of nearly-degenerate Floquet modes (e.g. ω_1 and $\omega_2 - \Omega$) and their coupling terms. As shown above, all these 2-by-2 matrices share the same Floquet eigenvalues, modulus Ω. Specifically, we can focus on one of them that reads:

$$\begin{pmatrix} \omega_2 - \Omega & -\Omega V_{21} \\ 0 & \omega_1 \end{pmatrix}\begin{pmatrix} c_{2,-1} \\ c_{1,0} \end{pmatrix} = \varepsilon \begin{pmatrix} 1 & V_{21} \\ V_{21}^{\star} & 1 \end{pmatrix}\begin{pmatrix} c_{2,-1} \\ c_{1,0} \end{pmatrix} \tag{6}$$

4

An equivalent way of writing the eigenvalue problem (6) is:

$$\frac{1}{1-|V_{21}|^2}\begin{pmatrix} \omega_2 - \Omega & -(\Omega + \omega_1)V_{21} \\ (\Omega - \omega_2)V_{21}^{\star} & \omega_1 + \Omega|V_{21}|^2 \end{pmatrix}\begin{pmatrix} c_{2,-1} \\ c_{1,0} \end{pmatrix} = \varepsilon \begin{pmatrix} c_{2,-1} \\ c_{1,0} \end{pmatrix} \tag{7}$$

It is evident that the two bands are decoupled as long as $V_{21} = 0$ and the corresponding eigenvalues are $\varepsilon_{1,2} = \omega_2 - \Omega, \omega_1$, respectively. In contrast, when $V_{21} \neq 0$, the new eigenvalues are

$$\varepsilon_{1,2} = \frac{|V_{21}|^2\Omega + \omega_1 + \omega_2 - \Omega \pm \sqrt{(|V_{21}|^2\Omega + \omega_1 + \omega_2 - \Omega)^2 - 4(1 - |V_{21}|^2)\omega_1(\omega_2 - \Omega)}}{2(1 - |V_{21}|^2)} \tag{8}$$

For on-resonance driving ($\Omega = \omega_2 - \omega_1$), the splitting of the two states is

$$\delta\varepsilon \approx 2|V_{21}|\sqrt{\omega_1\omega_2} \tag{9}$$

This is how we derived Eq. 2 in the main text. As shown, this eigenvalue problem is necessarily non-Hermitian but has real eigenvalues when $\omega_1\omega_2 > 0$.

Supplementary Note 4: Floquet photonic systems with and without time-reversal symmetry

In this section, we illustrate the conditions on preserving or breaking time-reversal (T) symmetry in a monochromatically driven nonlinear photonic crystal. Mathematically, T-symmetric means the matrix operator in the Floquet eigenvalue problem (4a) have the property of:

$$T(\hat{N}^{-1}\hat{M})_{\mathbf{k}}T^{-1} = (\hat{N}^{-1}\hat{M})^{\star}_{-\mathbf{k}} \tag{10}$$

When we look at individual terms of the matrices, it is easy to show that $T-$symmetry is equivalent to requiring:

$$V_{ij}(\mathbf{k}) = V_{ij}^{\star}(-\mathbf{k}), \tag{11}$$

5

where the coupling terms are defined as:

$$V_{ij}(\mathbf{k}) = \langle i, \mathbf{k} | V | j, \mathbf{k} \rangle. \tag{12}$$

Here i, j label the bands and $\bar{\bar{\epsilon}}_{\mathrm{nl}}(t) = V e^{-i\Omega t} + V^\dagger e^{i\Omega t}$ represents the effective permittivity tensor induced by the second-order optical nonlinearity of a material driven by an external electric field. As we started from a $T-$symmetric system in the static case, we have $|i, \mathbf{k}\rangle = |i, -\mathbf{k}\rangle^\star$. As a result, T can be broken in a second-order nonlinear optical material, when the coupling operator V is a complex tensor ($V \neq V^\star$). This can be achieved by driving the material with an elliptically polarized field. On the other hand, a linearly polarized field always lead to a real coupling operator, and the system is thus always T-symmetric.

Supplementary Note 5: Temporal analysis of the principle optical axes

Aside from the mathematical description of T-symmetry above, in this section, we provide an intuitive understanding on why some driving fields break T while others preserve T by analyzing the temporal evolution of the principle optical axes under a monochromatic driving field in an example material of LiNbO$_3$. Without driving field, LiNbO$_3$ is an uni-axial medium[2], where the principle optical axes - along which the permittivity tensor is diagonalzed - can be chosen as $(\hat{\mathbf{x}}, \hat{\mathbf{y}}, \hat{\mathbf{z}})$. In this coordinate, the permittivity tensor reads:

$$\bar{\bar{\epsilon}} = \begin{pmatrix} \epsilon_{xx} & 0 & 0 \\ 0 & \epsilon_{xx} & 0 \\ 0 & 0 & \epsilon_{zz} \end{pmatrix}. \tag{13}$$

Next we apply two specific examples of linearly and elliptically polarized drive, (1) x-polarized

and (2) circularly polarized, and analyze the evolution of instantaneous optical axes. Under an x-polarized driving field, $E_x^{\mathrm{d}} = E \cos \Omega t$, the only active second-order optical nonlinearity of LiNbO$_3$ is $\chi_{zxx}^{(2)}$ (d_{31}), which gives rise to two terms in the effective permittivity, ϵ_{xz} and ϵ_{zx}:

$$\bar{\bar{\epsilon}}_{\mathrm{eff}} = \begin{pmatrix} \epsilon_{xx} & 0 & \alpha \cos \Omega t \\ 0 & \epsilon_{xx} & 0 \\ \alpha \cos \Omega t & 0 & \epsilon_{zz} \end{pmatrix}, \tag{14}$$

where $\alpha = d_{31} E$. Limited by the material damage threshold[3], the induced nonlinear permittivity change is always small: $\beta = \alpha/(\epsilon_{xx} - \epsilon_{zz}) \ll 1$. As a result, diagonalizing the effective permittivity tensor in (14) yields the new optical principle axes in the driven medium:

$$\hat{\mathbf{e}}_1 = (0, 1, 0)^{\mathrm{T}} \tag{15}$$

with $\epsilon_1 = \epsilon_{xx}$;

$$\hat{\mathbf{e}}_2 = (1, 0, \beta \cos \Omega t)^{\mathrm{T}} \tag{16}$$

with $\epsilon_2 = \epsilon_{xx} + \alpha\beta \cos^2 \Omega t$; and

$$\hat{\mathbf{e}}_3 = (-\beta \cos \Omega t, 0, 1)^{\mathrm{T}} \tag{17}$$

with $\epsilon_3 = \epsilon_{zz} - \alpha\beta \cos^2 \Omega t$. In such cases, one optical axis of LiNbO$_3$ remains static $\hat{\mathbf{e}}_1 = \hat{\mathbf{y}}$; while the other two axes ($\hat{\mathbf{e}}_{2,3}$) are oscillating about z and x axes, respectively. Note these oscillations are T-preserving, which is easy to see as the substitution from t to $-t$ leaves all results unchanged.

On the other hand, under a circularly polarized driving field: $E_x^{\mathrm{d}} = E \cos \Omega t$ and $E_y^{\mathrm{d}} = E \sin \Omega t$, both $\chi_{zxx}^{(2)} = d_{31}$ and $\chi_{zyy}^{(2)} = d_{32}$ terms of LiNbO$_3$ are active, and the new effective

permittivity tensor reads:

$$\bar{\bar{\epsilon}}_{\text{eff}} = \begin{pmatrix} \epsilon_{xx} & 0 & \alpha\cos\Omega t \\ 0 & \epsilon_{xx} & \alpha\sin\Omega t \\ \alpha\cos\Omega t & \alpha\sin\Omega t & \epsilon_{zz,} \end{pmatrix} \tag{18}$$

where $\alpha = d_{31}E = d_{32}E$. Again limited by the material damage, $\beta = \alpha/(\epsilon_{xx} - \epsilon_{zz}) \ll 1$, and the new optical principle axes become:

$$\hat{\mathbf{e}}_1 = (-\sin\Omega t, \cos\Omega t, 0)^{\mathrm{T}} \tag{19}$$

with $\epsilon_1 = \epsilon_{xx}$;

$$\hat{\mathbf{e}}_2 = (\cos\Omega t, \sin\Omega t, \beta)^{\mathrm{T}} \approx (\cos\Omega t, \sin\Omega t, 0)^{\mathrm{T}} \tag{20}$$

with $\epsilon_2 = \epsilon_{xx} + \alpha\beta$; and

$$\hat{\mathbf{e}}_3 \approx (-\beta\cos\Omega t, -\beta\sin\Omega t, 1)^{\mathrm{T}} \tag{21}$$

with $\epsilon_3 = \epsilon_{zz} - \alpha\beta$. As shown, all three optical axes rotate around the z-axis at the driving frequency Ω, and it is exactly this spinning behavior that breaks T-symmetry.

Supplementary Note 6: Berry curvature and Chern number calculations for Floquet bands

In this section, we define the Berry curvature for the Floquet bands, and explain how Chern number is defined. First, we reduce the Floquet eigenvalue problem at each $\mathbf{k}$ point into a non-Hermitian matrix eigenvalue problem as shown in Supplementary Note 1. We define the Berry curvature solely based on the right eigenstates of this eigenvalue problem as the Chern number defined in this "Hermitian" way is the same as if we were to define it using both the left and right

eigenstates[4]. Specifically, we define Berry connection as:

$$\mathcal{A}_{\mathbf{k}} = -i \langle \Psi | \nabla_{\mathbf{k}} | \Psi \rangle \tag{22}$$

where Ψ are the column vectors that solve the matrix eigenvalue problem of (4a). Though this definition only uses the coefficients c_{jm}, the Chern number remains the same if we use the actual Floquet mode profiles of $c_{jm} | j, m \rangle$ as one can show the contributions from the cross terms $\langle j'm' | \nabla_{\mathbf{k}} | B_0 jm \rangle$ always add up to 0. Finally, we define Berry curvature as:

$$\mathcal{B}_{\mathbf{k}} = \nabla_{\mathbf{k}} \times \mathcal{A}_{\mathbf{k}}, \tag{23}$$

and define Chern number as the integral of $\mathcal{B}_{\mathbf{k}}$ over the entire Brilluion zone.

Next, we show two examples of the calculated Berry curvature of the Floquet bands. First we calculate for the T-symmetric example shown the previous section; specifically, we set $\Omega a / 2\pi c = 0.37$, which is close to the transition point of $\Omega_{\mathrm{C}}^{\mathrm{L}} = 0.3753$. As shown in Fig.2a, the calculated Berry curvature for the bottom band is indeed localized in $\mathbf{k}$ space next to the transition points. Furthermore, the Berry curvature is an odd function under C_2 rotation, which is the consequence of T-symmetry. Accordingly, the Chern number of the band is always zero.

In comparison, our second calculation is for the Floquet Chern insulator example show in the right panel of Fig.3d in the main text, with a modulation frequency $\Omega a / 2\pi c = 0.38$. As shown in Fig.2b, the Berry curvature is no longer an odd function in $\mathbf{k}$ space due to the absence of T-symmetry, while it is still localized near the transition point.

9

Supplementary Note 7: Super-cell setup for chiral edge state calculations

In this section, we present the super-cell setup in Fig. 4a in the main text, and explain how the edge and bulk states dispersion are calculated. First, we note that the external modulation applied in the domain-wall problem preserves translation symmetry in x direction, thus k_x is still a preserved quantity. Furthermore, by imposing periodic boundary condition along $1/2\hat{\mathbf{x}} + \sqrt{3}/2\hat{\mathbf{y}}$ direction, the trial solution of the Maxwell equation can be written in the form:

$$\Psi_{k_x}(t) = e^{ik_x x - i\varepsilon t} \sum_{j,m,k_y} c_{j,m,k_y} |j(k_x, k_y)\rangle \frac{e^{ik_y y}}{\sqrt{N}} e^{im\Omega t}$$

$$= e^{ik_x x - i\varepsilon t} \sum_{j,m,k_y} c_{j,m,k_y} |j, m, k_y\rangle \tag{24}$$

where $k_y = (\frac{n}{N}\frac{4\pi}{a} - k_x)/\sqrt{3}$, N is the number of unit cells contained in the super-cell and n is an integer runs from 0 to $N - 1$. It is easy to show that the basis states satisfy the orthonomal condition $\langle j', m', k_y' | B_0 | j, m, k_y \rangle = \delta_{j',j}\delta_{m',m}\delta_{k_y',k_y}$. Substitution of the trial solution back into (1) and multiply $\langle j', m', k_y' |$ from the left, we obtain similar result as (3) with increased basis dimension:

$$\sum_{j,m,k_y} c_{j,m,k_y}[(\omega_{j,k_y} + m\Omega)\delta_{j',j}\delta_{m',m}\delta_{k_y',k_y} + m'\Omega V_{j'k_y',jk_y}\delta_{m',m-1} + m'\Omega V_{j'k_y',jk_y}^\dagger \delta_{m',m+1}]$$

$$= \varepsilon \sum_{j,m,k_y} c_{j,m,k_y}(\delta_{j',j}\delta_{k_y',k_y}\delta_{m',m} + V_{j'k_y',jk_y}\delta_{m',m-1} + V_{j'k_y',jk_y}^\dagger \delta_{m',m+1}) \tag{25}$$

where $V_{j'k_y',jk_y} = \langle j', k_y' | V | j, k_y \rangle$ is the interacting matrix element that couples the orthogonal basis states:

$$V_{j'k_y',jk_y} = \frac{1}{N} \sum_{n=0}^{N-1} \int_{\text{unit cell}} d^2\mathbf{r} u_{j',k_y'}^\star V u_{j,k_y} e^{i(k_y - k_y')(y + na\sqrt{3}/2)} \tag{26}$$

where u_{j,k_y} is the periodic function of the electric fields. If the super-cell is subject to uniform external modulation, namely V is the same for each unit cell, there is no interface along y direction

and the interacting matrix element reads:

$$V_{j'k'_y,jk_y} = \frac{1}{N} \int_{\text{unit cell}} d^2\mathbf{r} u^\star_{j',k'_y} V u_{j,k_y} e^{i(k_y-k'_y)y} \sum_{n=0}^{N-1} e^{i(k_y-k'_y)na\sqrt{3}/2}$$

$$= \int_{\text{unit cell}} d^2\mathbf{r} u^\star_{j',k_y} V u_{j,k_y} \delta_{k'_y,k_y} \tag{27}$$

On the other hand, when the super-cell consists of two regions (range from 0 to s and $s+1$ to $N-1$, respectively) being modulated with distinct polarization (V_1 and V_2), as the domain-wall problem considered in the max text, contributions from the two regions must be taken into account accordingly,

$$V_{j'k'_y,jk_y} = \frac{1}{N} \int_{\text{unit cell}} d^2\mathbf{r} u^\star_{j',k'_y} V_1 u_{j,k_y} e^{i(k_y-k'_y)y} \sum_{n=0}^{s} e^{i(k_y-k'_y)na\sqrt{3}/2}$$

$$+ \frac{1}{N} \int_{\text{unit cell}} d^2\mathbf{r} u^\star_{j',k'_y} V_2 u_{j,k_y} e^{i(k_y-k'_y)y} \sum_{n=s+1}^{N-1} e^{i(k_y-k'_y)na\sqrt{3}/2} \tag{28}$$

Therefore, the corresponding eigenvalue ε and eigenstate $\{c_{j,m,k_y}\}^{\mathrm{T}}$ for each k_x can be obtained by diagonalizing the Floquet Hamiltonian (25) in a similar way as we solve for the Floquet bulk spectrum in Supplementary Note 1.

Supplementary Note 8: Estimation of Floquet band gap size

In this section, we analyze the Floquet band gap size that can possibly be achieved with realistic nonlinear materials like LiNbO$_3$. From (9), it is found the induced Floquet gap size (normalized to $\sqrt{\omega_1\omega_2}$) by an external monochromatic drive is $\sim |V_{21}|$, which characterizes the coupling strength of the two modes mediated by the second order nonlinear process. For example,

when we consider the coupling between a TM ($|1\rangle$) and a TE mode ($|2\rangle$), it reads

$$
\begin{aligned}
|V_{21}| &= \int d^2\mathbf{r} \mathbf{E}_{\text{TE}}^{\star} \bar{\bar{\epsilon}}_{\text{nl}} \mathbf{E}_{\text{TM}} \\
&= \frac{\epsilon_{xz}}{\epsilon_1} \int d^2\mathbf{r}\epsilon_1 E_{x,\text{TE}}^{\star} E_{z,\text{TM}} + \frac{\epsilon_{yz}}{\epsilon_1} \int d^2\mathbf{r}\epsilon_1 E_{y,\text{TE}}^{\star} E_{z,\text{TM}}
\end{aligned}
\tag{29}
$$

where the integral is performed over the area filled with nonlinear materials and $\epsilon_{xz}, \epsilon_{yz}$ terms are the effective permittivity induced by external drive. Limited by the material damage threshold, the maximal value of $\epsilon_{xz,yz}/\epsilon_1$ for LiNbO$_3$ is estimated to be $\sim 5 \times 10^{-3}$. On the other hand, the modal overlap integral depends on the choice of bands and may varies from 10^{-2} to 1. As a result, the normalized Floquet gap size is typically on the order of $5 \times 10^{-5} \sim 5 \times 10^{-3}$.

To clearly show the Floquet gap in Fig. 3 in the main text, we assume large effective permittivity for both elliptically and linearly polarized drive: $(\epsilon_{xz}, \epsilon_{yz}) = (2, -1.08 + 1.9i)$ and $(\epsilon_{xz}, \epsilon_{yz}) = (-0.26, 2)$, respectively. The resulted gap size is $\sim 10^{-2}$. Therefore, we expect to obtain a gap size of $\sim 10^{-4}$ when the driving field strength is reduced by 100 times (4 GV·m^{-1}), which is below the material damage threshold. Similarly, for the chiral state dispersion calculation, we also assume large effective permittivity for the normal insulators: $(\epsilon_{xz}, \epsilon_{yz}) = (3, 1)$, which support a frequency gap aligned with the gap of the Chern insulator.

Supplementary References

1. Rudner, M. S., Lindner, N. H., Berg, E. & Levin, M. Anomalous edge states and the bulk-edge correspondence for periodically driven two-dimensional systems. *Physical Review X* **3**, 031005 (2013).

2. Boyd, R. W. *Nonlinear optics* (Elsevier, 2003).

3. Bach, F., Mero, M., Chou, M.-H. & Petrov, V. Laser induced damage studies of linbo 3 using 1030-nm, ultrashort pulses at 10-1000 khz. *Optical Materials Express* **7**, 240–252 (2017).

4. Shen, H., Zhen, B. & Fu, L. Topological band theory for non-hermitian hamiltonians. *Physical review letters* **120**, 146402 (2018).
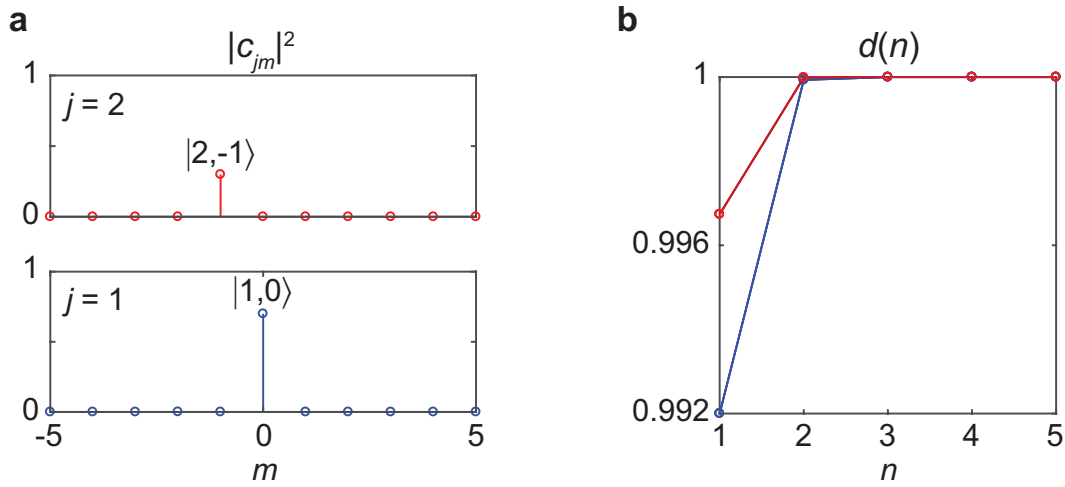
Supplementary Figure 1: | **The convergence of Floquet eigenstates calculation with truncated Floquet basis. a,** The localization of c_{jm} in m for a specific Floquet state (the bottom band at the Γ point in Fig.3d of the main text). **b,** The convergence of $d(n)$ for the two Floquet bands in Fig.3d of the main text.
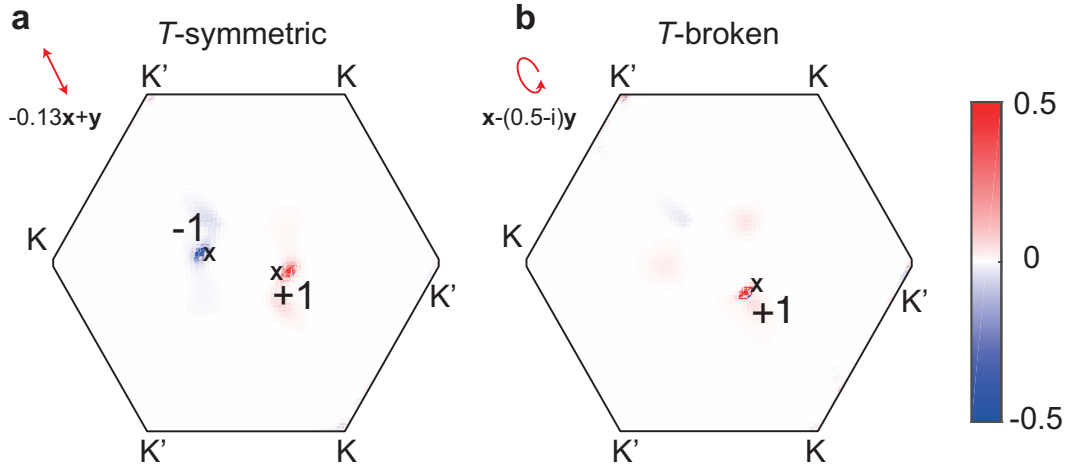
Supplementary Figure 2: | **Berry curvature distributions of Floquet bands with and without time-reversal symmetry. a,** Under linearly polarized drive, the calculated Berry curvature is an odd function of **k** and is localized near the two Weyl points (cross) due to the presence of time-reversal symmetry. **b,** In contrast, when the photonic crystal is driven by elliptically polarized light, as the case shown in Fig.3d of the main text, $\mathcal{B}_{\mathbf{k}}$ is no longer an odd function of **k**, while it is still localized near the phase transition point (cross).